“Empirical pre-whitening” spectral analysis detects periodic but inconsistent signals in abyssal hill morphology at the southern East Pacific Rise

John A. Goff

University of Texas Institute for Geophysics, Austin, Texas, USA

Key Points:

1. A new algorithm is formulated to detect periodicities embedded in an aperiodic process using “empirical pre-whitening” spectral analysis
2. Periodicities are detected at the southern East Pacific Rise, but are spatially and temporally inconsistent
3. The dominant aperiodic signal is likely fault-constructed, while ephemeral periodic signals may relate to internal melt supply variations

Abstract. The existence, or not, of periodicities in abyssal hill morphology has been vigorously debated in recent publications, and some have hypothesized that such periodicities are evidence of the impact of Milankovitch cycle-caused sea level fluctuations on the volcanic construction process at mid-ocean ridges. Periodicities are detected by the presence of spectral peaks that rise significantly above the random variations of sample power spectra associated with an aperiodic, continuous spectrum process, typically modeled as a band-limited fractal (von Kármán model). Here I formulate and test a new algorithm to "empirically pre-whiten" the sample power spectrum which, without needing to model the continuous spectrum, flattens it to a zero-mean process. This greatly simplifies definition of the null hypothesis, and additional modeling approximates standard deviation levels that provide a conservative basis for detecting peaks that may be indicative of periodicity. The algorithm is applied to extensive bathymetric data flanking the southern East Pacific Rise. Significant periodicities are detected on many profiles analyzed, but the periods vary widely, and do not cluster at Milankovitch periods. The most substantial harmonic signals detected exhibit periods ~0.082-0.216 my, with root-mean square (RMS) heights approximately a quarter to a third of the RMS height for the aperiodic signal. It is hypothesized that the dominant aperiodic component of abyssal hills corresponds to morphology constructed by faults that follow a random distribution governed by scaling laws, whereas longer-scale periodic signals are associated with crustal thickness variations controlled internally by variations in melt supply.

Key Words: Mid-ocean ridge, faulting, melt supply, von Kármán model, stochastic processes, autocovariance

1. Introduction

A number of recent publications have endeavored to identify peaks in the sample power spectra (periodograms) of abyssal hill bathymetry profiles, presumably indicative of periodicities that could be interpreted as systemic temporal variations in mid-ocean ridge (MOR) processes (Crowley et al., 2015; Tolstoy, 2015; Olive et al., 2016; Shinevar et al., 2019). Discovery of topographic periodicities would greatly impact our understanding of variability in MOR processes, whether externally forced, such as proposed Milankovitch Cycle dependence (Crowley et al., 2015; Tolstoy, 2015), or internally forced, such as via modulations of mantle upwelling (Shinevar et al., 2019; Parnell-Turner et al., 2020). There are, however, a number of potential pitfalls in these analyses, and it is quite possible that the spectral peaks that have been discerned are instead typical random fluctuations of a sample power spectrum estimated from an aperiodic time series, particularly if detection thresholds are not sufficiently conservative.

As described in Priestley (1981), there are two end-member time series spectra: discrete and continuous. Discrete spectra are those with one or more periodicities, detected by peaks on the sample power spectrum at individual frequencies. Well-known methods are established for determining the significance of those peaks as observed on a sample power spectrum in the presence of a background white noise process. In contrast, continuous spectra processes are those that are characterized by a smooth, continuous power spectral function $P(f)$ across a range of frequencies, f, and do not contain any periodicities. However, sample power spectra derived from continuous-spectra time series are, in Priestley's (1981) words, "erratic and wildly fluctuating", which is a result of two well-known properties: (1) the variance of the sample power spectrum does not approach zero as the number or sample points (N) approaches infinity, and (2) the correlation between two sample power spectrum points decreases as N increases. Because of this erratic property, application of discrete-spectrum tests to continuous-spectra processes "may indicate the existence of a large number of spurious periodic components",

according to Priestley (1981); the methods are not invalid, he states, but rather are misapplied when used on time series with continuous spectra. Furthermore, since the variance of the sample power spectrum scales with $P^2(f)$, such false detections are more likely where $P(f)$ is larger.

Between the discrete and continuous spectrum end members, Priestley (1981) describes a "mixed" spectrum derived from the blending of time series of both periodic and aperiodic character, which is an apt model for hypothesizing the existence of periodicities in abyssal hill morphology (Goff et al., 2018). Abyssal hills are formed primarily by normal faults (McDonald et al., 1996; Durant et al., 1996; Macdonald, 2015), whose throw and spacing can be modeled as random distributions that follow scaling laws (Malinverno and Cowie, 1993; Bohnenstiehl and Carbotte, 2001). Abyssal hill morphology statistical properties have been successfully characterized using a von Kármán functional form (von Kármán, 1948), a continuous (aperiodic) spectrum that can also be described as a band-limited fractal model (Goff and Jordan, 1988, Goff and Tucholke, 1997). Any periodic component of the seafloor topography, such as might be caused by variations in crustal thickness, independent of the abyssal hill faulting process, could be modeled as a superposition of periodic and aperiodic signals.

If we consider the aperiodic time series with continuous power spectrum, $P(f)$, to be a null hypothesis, rejection of the null hypothesis would be established by observation of a spectral peak that greatly exceeds the normal variation of the continuous sample power spectrum. However, to do this, the null hypothesis must be defined, which requires either knowing $P(f)$ *a priori*, or modeling $P(f)$ by fitting a functional form (e.g., Goff and Jordan, 1988). Vaughan (2005), for example, formulated a methodology for detecting periodicities in the presence of a red (negative trend with frequency) background noise, which can be fit with simple power-law, and where the null hypothesis variability about this trend is characterized by a χ^2 distribution. Vaughan (2005) noted, however, that the modeling fit itself adds additional uncertainty, leading him to strongly suggest that confidence levels 3-4 times the standard deviation (σ) should be applied when determining the significance of a spectral peak

in indicating a periodic component of a mixed spectrum, rather than the oft-assumed 2σ confidence level.

Pre-whitening is another approach to assisting in the detection of periodicities in a mixed spectrum; the general idea is to divide the sample power spectrum by $P(f)$ so that the overall trend is flat; i.e., it emulates a discrete spectrum in the presence of white noise. In this construction, standard tests for the significance of observed peaks can be applied (Priestley, 1981). The spectral analysis methodology employed by Crowley et al. (2015) and emulated by others (Olive et al., 2016; Shinevar et al., 2019), does indeed attempt to apply pre-whitening to the spectrum. However, no attempt was made in these analyses to estimate $P(f)$, applying instead simple f^2 multiplicative factor that fails to flatten the spectrum. Rather, because abyssal hills are band-limited in their power-law (i.e., fractal) behavior, this attempt at pre-whitening causes the spectrum to arc, artificially enhancing positive spectral fluctuations near the apex of the arc to appear more significant than they likely are. Although modeling the spectrum using the von Kármán function would undoubtedly improve pre-whitening, Priestley (1981) argues against pre-whitening in this way because, if there is indeed a periodic component, it will distort the modeling of $P(f)$ in a way that adversely affects both that estimation and the ultimate detection of periodic signals.

Harmonic components of a mixed spectrum profile can also be detected using multitaper techniques (Thomson, 1990; Percival and Walden, 1993; Mann and Lees, 1996; Crowley et al., 2015). Multitaper spectral estimation applies an orthogonal series of tapers to a time series, Fourier transforms each and then adds the results together to form a sample power spectrum. This technique is widely used to reduce the variability of the power spectrum estimate in comparison to the periodogram, and eliminate spectral leakage (e.g., McCoy et al., 1998; Babadi and Brown, 2014). An embedded harmonic signal may be detected by an F-test for phase-coherent variability at any one frequency across taper components (Thomson, 1990; Mann and Lees, 1996). However, phase coherence does not necessarily imply

115 significance with respect to the variability associated with the aperiodic component of the process at
116 that frequency (Mann and Lees, 1996). Alternatively, or in addition to the F-test, the height of a spectral
117 peak can be compared against an assumed χ^2 distribution on local variability about the null hypothesis,
118 which is represented by the best estimate of $P(f)$ for the multitaper estimate of the power spectrum
119 (Percival and Walden, 1993; Mann and Lees, 1996; Crowley et al., 2015). This test is akin to the
120 procedure Vaughan (2005) utilized for the periodogram.

121 To obviate the need to model $P(f)$ for defining the null hypothesis and/or for pre-whitening,
122 Priestley (1981; Chapter 8) proposed an ingenious and simple solution that he termed the "P(λ)" test.
123 The method utilizes the sample autocovariance function, which is the Fourier transform pair of the
124 sample power spectrum. The sample autocovariance consists of two components: (1) a central,
125 decaying portion that includes all information about the functional nature of the continuous, aperiodic
126 spectrum $P(f)$, and (2) a long tail that randomly fluctuates about 0 and, should they be present, also
127 includes harmonic fluctuations associated with periodic components of the time series because they do
128 not decay to zero with increasing lag. Priestley's (1981) method consists of zeroing-out the central,
129 decaying portion of the sample autocovariance (which can be determined by simple inspection rather
130 than modeling), and then Fourier-transforming the remaining tails; the result will be a zero-mean (null
131 hypothesis), randomly fluctuating function, with positive spikes at frequencies if and where periodic
132 signals are present (deviation from null hypothesis). Despite the relative simplicity and elegance of the
133 P(λ) test, a literature search found very few examples of its application (e.g., Bhansali, 1977; Garrido and
134 Garcia, 1992). For clarity in terminology, I propose the term "empirical pre-whitening" to describe this
135 simple technique.

136 In this paper I present a new algorithm for utilizing Priestley's (1981) "P(λ)"/empirical pre-whitening
137 method to detect periodic signals in a mixed-spectra process. I first test the algorithm on synthetic
138 profiles generated by adding cosine functions of various amplitude and frequency to an aperiodic time

series corresponding to the von Kármán statistical model (Goff and Jordan, 1988). The algorithm is able to accurately detect the periodic components provided the amplitude is sufficient to rise significantly above the random fluctuations associated with the aperiodic component of the spectrum at that frequency. I then apply this algorithm to twelve bathymetric profiles of abyssal hill morphology along the southern East Pacific Rise (EPR) to test for the presence of periodicities. A portion of this region was also used by Tolstoy (2015) in a spectral analysis that discerned a ~100 ky periodicity, which is one of the Milankovitch periods. The profiles are converted from distance to crustal age versus depth using an existing, high-resolution age model for the region (Goff et al., 2018).

2. Formulation

The following formulation is based on Priestley (1981; Section 8.4). Consider a discrete time or space series X_i, $1 \le i \le N$, evenly space by ΔX. Consider further that X_i represents the summation of two independent, zero-mean, stationary processes Y_i and Z_i, where Y_i is an aperiodic process with a continuous spectrum, and Z_i is represented by one or more sinusoidal forms. The autocovariance of X_i, $R_x(s)$, is then represented by:

$$E[X_i X_{i+s}] = R_X(s) = R_Y(s) + R_Z(s), \quad (1)$$

where E[] is the expectation operator, s is the lag index, and $R_Y(s)$ and $R_Z(s)$ are the autocovariances of Y_i and Z_i, respectively. Because Y_i is aperiodic, $R_Y(s)$ will decay monotonically with increasing $|s|$. Because Z_i has periodic elements, $R_Z(s)$ will also vary sinusoidally for all s; each sinusoidal element, defined by a frequency f amplitude and amplitude α, will contribute a term $\frac{1}{2}\alpha^2 \cos(2\pi s f)$ to $R_Z(s)$. The sample autocovariance, i.e., estimation of $R_x(s)$ based on samples X_i, is given by:

$$\hat{R}_X(s) = \frac{1}{N-s}\sum_{i=1}^{N-s} X_i X_{i+s}, \quad 0 \le s \le N/2$$

$$\hat{R}_X(-s) = \hat{R}_X(s). \quad (2)$$

The power spectrum of X_i, denoted by $P_X(f)$, is the Fourier transform conjugate of $R_x(s)$, and we can likewise define the power spectra of Y_i and Z_i in the same way such that

$$P_X(f) = P_Y(f) + P_Z(f). \quad (3)$$

The sample power spectrum can be computed in two equivalent ways:

$$\hat{P}_X(f) = DFT\left[\hat{R}_X(s)\right], \text{ or} \quad (4)$$

$$\hat{P}_X(f) = |DFT[X_i]|^2 \quad , \quad (5)$$

were DFT indicates the discrete Fourier transformation. Equation (5) is far more commonly utilized since it does not require the extra step of computing the sample autocovariance as in Equation (2). However, Equation (4) is utilized here because it provides a mechanism for separating periodic from aperiodic components of the spectrum. Priestley (1981) proposes in his "$P(\lambda)$" test to first inspect $\hat{R}_X(s)$ after computing it in order to identify a value m such

$$R_Y(s) \sim 0, |s| \geq m. \quad (6)$$

In other words, we seek to identify that portion of the sample autocovariance which is monotonically decaying, and which contains all the structural information that constrains the continuous portion of the power spectrum $P_Y(f)$. The remainder, or "tail," is a zero-mean signal that, if there are no periodic elements in X_i, will fluctuate randomly (and which, after DFT, contributes to the erratic fluctuations of $\hat{P}_X(f)$). If, however, there are periodic elements, then those will be present in the tail, as noted above. The next step in Priestley's (1981) method is thus to remove the monotonically decaying portion of $\hat{R}_X(s)$ by zeroing it out for $|s| < m$:

$$\hat{R}_X^m(s) = \begin{cases} 0, & |s| < m \\ \hat{R}_X(s), & |s| \geq m \end{cases} \quad . \quad (7)$$

Finally, this altered sample autocovariance is transformed to create the "empirically pre-whitened" spectrum

$$\hat{P}_X^m(f) = DFT\left[\hat{R}_X^m(s)\right]. \quad (8)$$

In practice, the "cut" edges at $|\pm s| = m$, as well as the ends of the function at $|\pm s| = N/2$, need to be tapered prior to the DFT in order to minimize spectral leakage.

In the case of the null hypothesis, where no periodicity is present and $P_X(f) = P_Y(f)$, Priestly (1981) demonstrates that

$$\mathrm{E}\left[\hat{P}_X^m(f)\right] = 0, \tag{9}$$

and

$$VAR\left[\hat{P}_X^m(f)\right] \sim \frac{N-2m}{2} P_Y^2(f)\,, \tag{10}$$

where VAR indicates the variance. Therefore, the standard deviation on the null hypothesis, σ, is estimated by the square root of Equation (10). Deviation from the null hypothesis can be established by observation of spectral peaks that significantly deviate from the typical erratic variability associated with the continuous component of the spectrum. For this purpose, a conservative criterion must be applied. Depending on N, the empirically pre-whitened spectrum could have hundreds or thousands of peaks and valleys, so that numerous peaks are expected to surpass a 2σ (95%) threshold, and even several are likely to surpass a 3σ (99%) threshold without the presence of a periodic signal. In the following analyses, a value of 3.5σ will be used as a minimum detection threshold.

Equation (10) does require knowledge of the underlying continuous spectrum $P_Y(f)$. Where $P_Y(f)$ is not known *a priori*, it must be modeled by fitting a smooth functional form to the sample autocovariance or sample power spectrum. This will be demonstrated in Section 4. Addition of periodic components will increase the overall variance of the profile compared to the null hypothesis, thus increasing the modeled value of $P_Y(f)$ and subsequent estimation of σ. Fortunately, this has the effect of increasing the confidence in detection of periodic contributions, since the level of significance of a spectral peak should be considered a minimum value.

3. Synthetic Test

To test the ability of an empirically pre-whitened spectrum to detect periodic elements of a mixed spectrum process, I constructed a series of synthetic profiles consisting of the addition of an aperiodic time series, generated from the von Kármán statistical model, and cosine functions of varying amplitude and frequency. The von Kármán statistical model can be expressed equivalently in either autocovariance or power spectral form (Goff and Jordan, 1988; Goff and Tucholke, 1997). For the autocovariance:

$$R_{VK}(s) = H^2 G_\nu[k_0 s]/G_\nu(0) \tag{11}$$

where H is the RMS height, k_0 is a scaling parameter with dimensions time^{-1} (or distance^{-1}), and G_ν is defined by

$$G_\nu(x) = x^\nu K_\nu(x).\ 0 \le x < \infty. \tag{12}$$

K_ν is the modified Bessel function of the second kind and order ν. At $\nu = ½$, $R_{VK}(s)$ is an exponential function. The functional form of the von Kármán power spectrum for a profile is given by:

$$P_{VK}(f) = \frac{\Gamma\left(\nu+\frac{1}{2}\right)}{\Gamma(\nu)} \frac{2H^2\sqrt[2]{\pi}(k_0/2\pi)^{2\nu}}{((k_0/2\pi)^2 + f^2)^{\nu+\frac{1}{2}}} \tag{13}$$

where Γ is the gamma function. In the power spectral formulation, $k_0/2\pi$ serves as a corner frequency: for $f \gg k_0/2\pi$, $P_{VK}(f)$ is a power-law form (i.e., red spectrum, or fractal), while for $f \ll k_0/2\pi$, $P_{VK}(f)$ is a constant (i.e., white spectrum). The order parameter ν determines the Haussdorf, or fractal dimension:

$$D = \mathrm{E} + 1 - \nu, \tag{14}$$

were E is the Euclidian dimension (i.e., E = 1 for a profile).

A synthetic profile conforming to the von Kármán statistical model can be generated by: (1) multiplying the amplitude spectrum (square root of Equation (13)) by a random phase $\exp(i\phi)$, where ϕ is a uniform random value distributed on $(0,2\pi]$, (2) enforcing Hermetian symmetry over negative

frequencies, and (3) transforming to the space domain by DFT (Goff and Jordan, 1988; Goff, 1995). The uniform random phase results in a Gaussian distribution of profile values. In practice, a larger profile than required should be generated, and then cropped to size in order to fully randomize the sample power spectrum of the synthetic profile.

For the synthetic experiment, parameters chosen were: H = 1 u_h, k_0 = 1 u_d^{-1}, and ν = 0.8, where u_h and u_d are arbitrary units of height and distance (or time), respectively. The profile length is 10,000 points with a node spacing of ΔX = 0.05 u_d. The top profile of Figure 1 displays the profile generated with these parameters. To generate a mixed-spectrum profile, $X_M(i\Delta X)$, I superpose cosine functions on the von Kármán profile using:

$$X_M(i\Delta X) = X_{VK}(i\Delta X) + \alpha[\cos(i\Delta X 2\pi f_1) + \cos(i\Delta X 2\pi f_2) + \cos(i\Delta X 2\pi f_3)]\,, \qquad (15)$$

where $X_{VK}(i\Delta X)$ is the profile generated with the von Kármán statistical model, and f_1, f_2 and f_3 are frequencies chosen to be 0.02, 0.1, and 0.5 cycles/u_d, respectively. Figure 1 displays the results of Equation (15) for values of α ranging from 0 to 0.5. A surprising observation regarding these profiles is that they look very similar; i.e., that the harmonic components are not visually self-evident, even at the largest value of α. This observation can be understood by considering the contribution of each sinusoidal component to the overall RMS height. For example, at α = 0.3 u_h, the variance is of the sinusoidal component is $\frac{1}{2}\alpha^2$, or 0.045 u_h^2. Added to the aperiodic variance of 1 u_h^2, the combined variance is 1.045 u_h^2, and taking the square root yields an overall RMS of 1.022 u_h. Thus, the addition of one sinusoidal component of amplitude 0.3 u_h increases the RMS by only 2.2%.

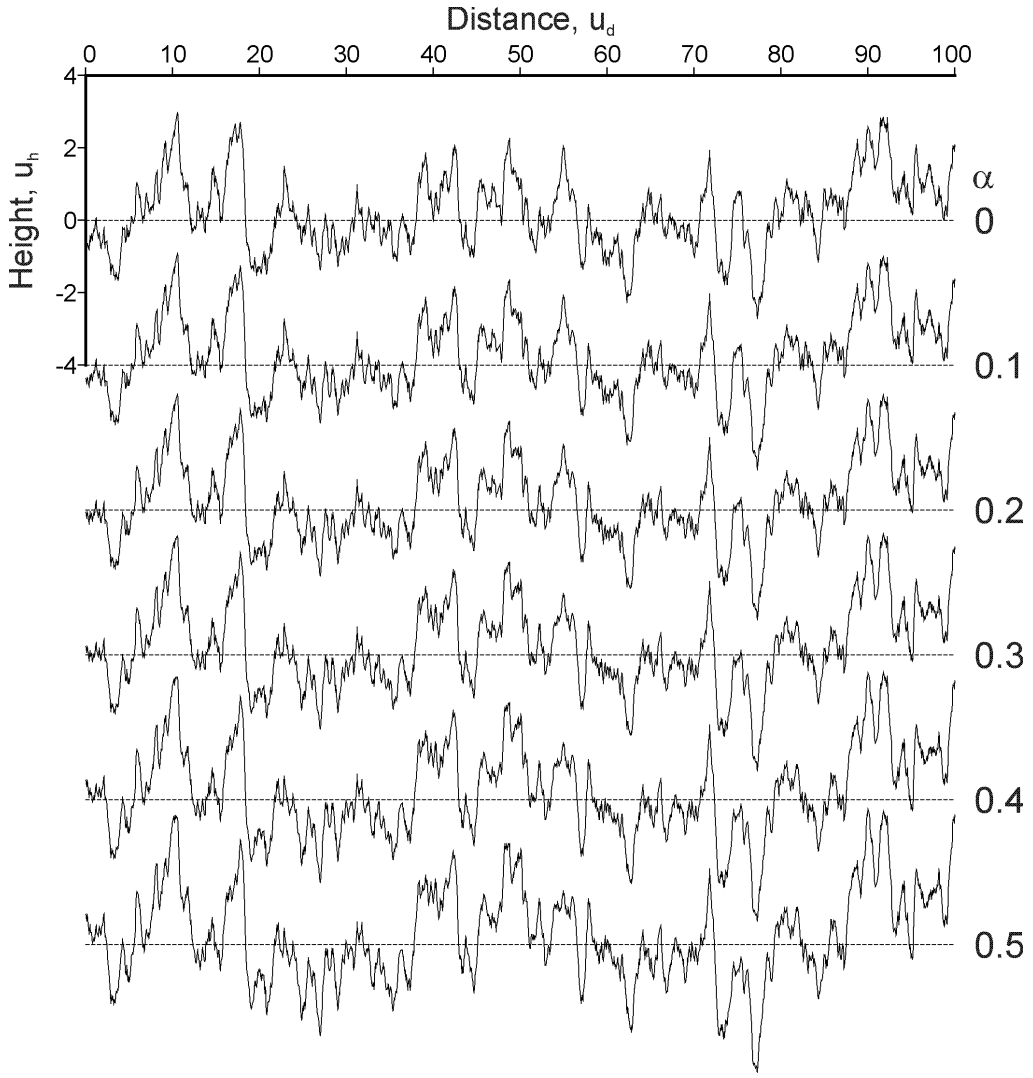

Figure 1. Synthetic profiles constructed using Equation (15) and parameters listed in the text. The vertical scale corresponds to the $\alpha = 0$ profile; all others are offset a constant distance for visualization. The first 100 u_d of each synthetic profile, out of a total distance of 500 u_d, are plotted.

In contrast to the profiles, the sample autocovariances of these profiles (Figure 2) display clear visual evidence of the harmonic components, which come to dominate the tails as *a* increases because they do not decorrelate as lag increases, as the aperiodic signal does. This is a clear visual confirmation of the utility of the sample autocovariance to isolate the harmonic components of a mixed spectrum process from the aperiodic components. Using these sample autocovariances, I have conducted a spectral analysis where I compare (1) the sample power spectrum computed by DFT of the full sample autocovariance, and (2) the empirically pre-whitened spectrum computed by DFT of the sample

autocovariance after zeroing-out the shaded regions shown in Figure 2, which self-evidently includes the full span of the monotonically-decaying portion of the function. In addition, a $\cos^2$ taper is applied over 10% of the profile at each edge to suppress spectral leakage. The full suite of results is presented in the Supplementary Material, and cases $\alpha = 0$ u_h and $\alpha = 0.3$ u_h are presented in Figures 3 and 4, respectively, to illustrate key findings.

The null ($\alpha = 0$ u_h) case is presented in Figure 3. As noted earlier, the von Kármán statistical model is a band-limited fractal, following a power-law form (negative linear trend on a log-log plot) at high frequencies, and flat at low frequencies, with the transition governed by the corner frequency. The sample power spectrum from the synthetic profile (Figure 3a) closely follows this functional form, as expected, but with the highly erratic variability that is characteristic of continuous-spectrum, aperiodic profile. The empirically pre-whitened spectrum for the null case (Figure 3b), is also highly erratic, but with a mean of zero which indicates success in removing the structural form of the continuous power spectrum. Comparison between Figures 3a and 3b demonstrates that the variations of the sample power spectrum about the model function are retained in the variation of the empirically pre-whitened spectrum about zero. The 2σ upper bound does well in characterizing the envelope of variability, which increases as f decreases, but is not a hard limit; at least two peaks are observed to exceed 2σ, which is expected statistically.

The $\alpha = 0.3$ u_h case is presented in Figure 4. Frequency f_3 (0.5 cycles/u_d) is detectable at $\alpha = 0.1$ u_h (Supplementary Material) owing to the fact that the variations of the aperiodic component of the profile are very small at this frequency. Frequencies f_1 (0.02 cycles/u_d) and f_2 (0.1 cycles/u_d), however, are only detectable at $>3.5\sigma$ for $\alpha = 0.3$ u_h (Figure 4b) and larger (Supplementary Material). Because they all have the same amplitude, the peaks at all three frequencies are expected to be of the same height on the empirically pre-whitened spectrum. However, the peak at f_2 is observed to be less than the peaks at f_1 and f_3 by about 25% (Figure 4b). This emphasizes an important point: the height of the discrete

spectral peaks are modulated by the random highs and lows of the continuous spectrum upon which it is superposed, leading to uncertainty in detection and measurement of amplitude (which will be considered in the next section).

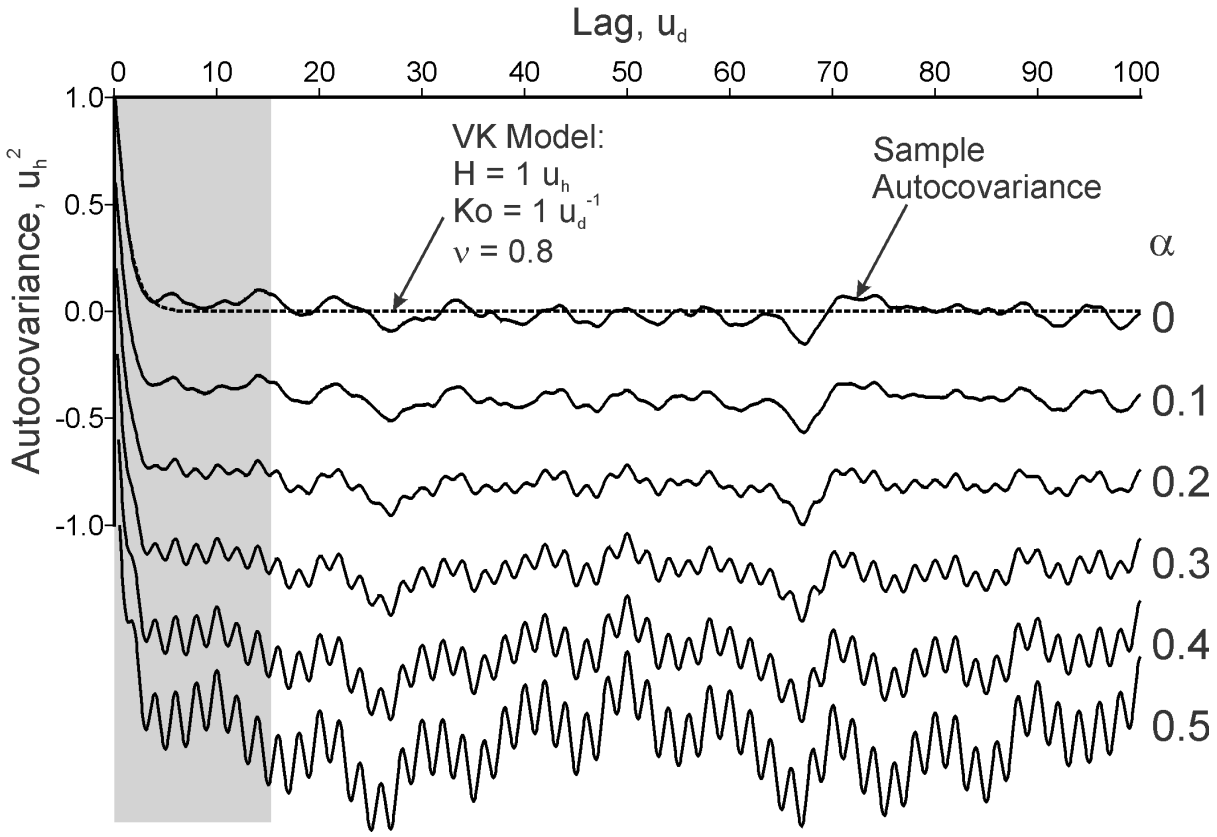

Figure 2. Sample autocovariance functions (solid) computed from profiles shown in Figure 1, plotted to a lag of 100 u_d. The von Kármán (VK) statistical model autocovariance, from which the synthetic profiles were generated, is overlain (dashed). The vertical scale corresponds to the $\alpha = 0$ function; all others are offset a constant distance for visualization. For Figures 3 and 4, the discrete Fourier transformation of the sample autocovariance (with Hermetian symmetry) is used to compute the sample spectral density, while the empirically pre-whitened spectrum is computed in the same way after values in the shaded region are zeroed out. The number of values zeroed out is determined by inspection, ensuring that the full span of the decaying portion of the autocovariance is removed and leaving only a fluctuating, zero-mean tail. A value of $\alpha = 0$ is the null condition of no periodic component to the sample profile. Periodic components come to dominate the tail of the autocovariance with increasing α, compared to the far more subtle visual impact evidenced in the synthetic profiles of Figure 1.

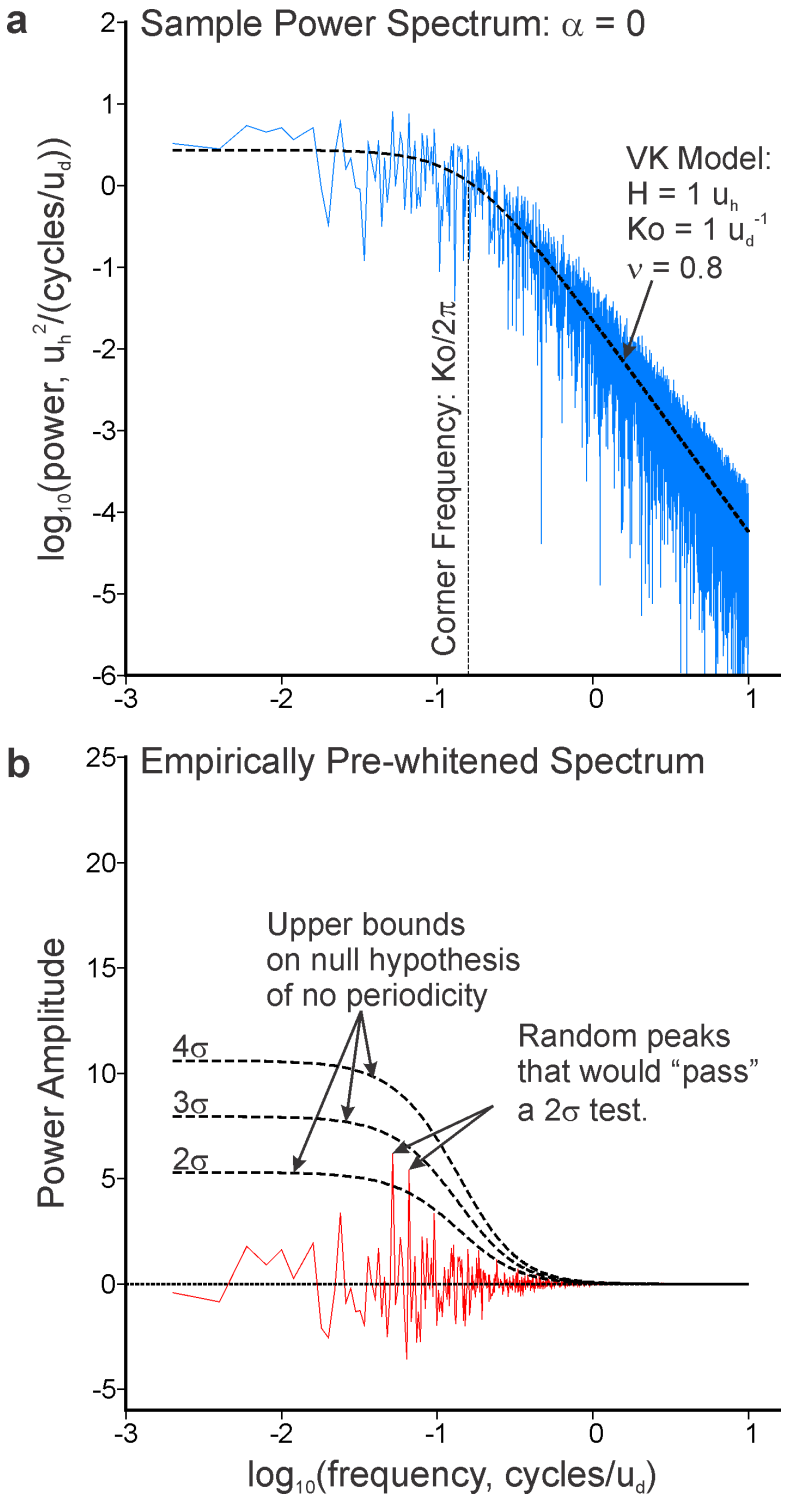

303

304 Figure 3. (a) Sample power spectrum and (b) empirically pre-whitened spectrum calculated from the $\alpha =$
305 0 sample autocovariance shown in Figure 2. The von Kármán model is overlain on the power spectral
306 density, and the 2σ, 3σ, and 4σ upper bounds on the null hypothesis are overlain on the empirically pre-
307 whitened spectrum. Examples of "false positive" detection of periodic components are observed in the
308 if the 2σ bound is used as a threshold.

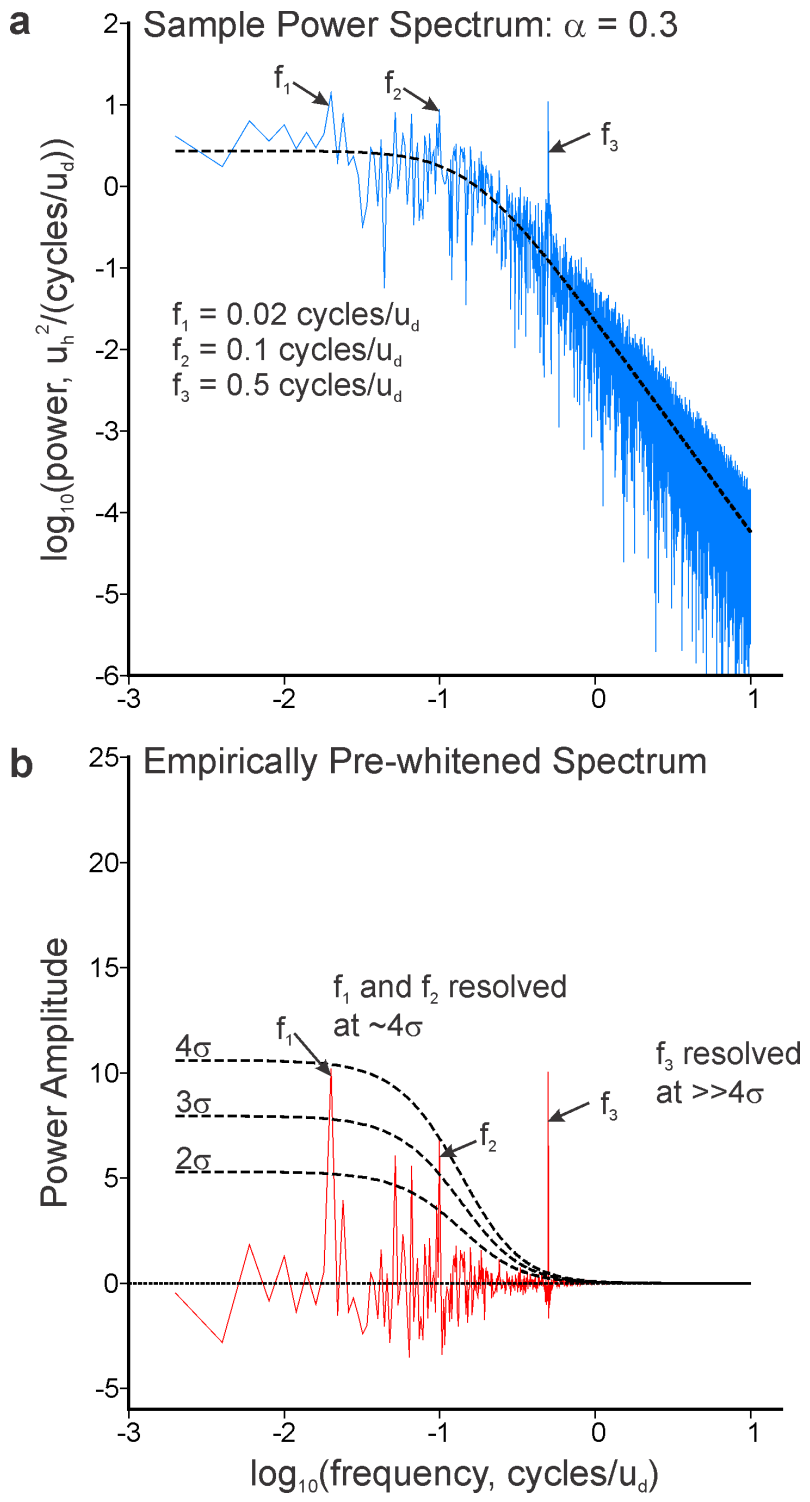

Figure 4. (a) Sample power spectrum and (b) empirically pre-whitened spectrum calculated from the α = 0.3 sample autocovariance shown in Figure 2. The von Kármán model is overlain on the power spectral density, and the 2σ, 3σ, and 4σ upper bounds on the null hypothesis are overlain on the empirically pre-whitened spectrum. All three harmonic components are resolved at > 3.5σ in this example.

This synthetic experiment demonstrates the efficacy of the empirically pre-whitened spectrum in detecting periodic components of a mixed spectrum profile. Even with a conservative detection criterion of 3.5σ, positive identification was made of harmonic signals that add only 2.2% each to the overall RMS variability. The certainty of detection increases as the amplitude of the sinusoidal component increases (Supplementary Material), providing confidence that any substantial harmonic component to the profile will be detected. The empirical pre-whitening algorithm has the potential for a wide variety of applications.

4. Application to the Southern East Pacific Rise

The southern East Pacific Rise (Figure 5) is the site of some of the most extensive publically-available multibeam bathymetric coverage in the world of a mid-ocean ridge (MOR) and its flanks (Scheirer et al. 1996). The region also exhibits some of the fastest MOR spreading rates (~7.7-7.8 cm/yr half rates DeMets et al., 1990). Tolstoy (2015) applied a spectral analysis in a limited area of this region and found a spectral peak at a period of ~100 ky, inferring that Milankovitch cycles may be influencing volcanic construction at the MOR. Goff et al (2018) further fine-tuned the Müller et al. (2016) age model for this region, and applied a stacking analysis to identify any temporal variations in bathymetry that were coherent across the region, which would be expected if the rise and fall of sea-level associated with Milankovitch cycles, and external forcing, were controlling abyssal hill construction. They found, however, that there was no evidence for spatially coherent temporal signals, periodic or otherwise. Nevertheless, lack of synchronicity does not imply lack of periodicity. Rather than an external forcing that affects the MOR uniformly either globally or regionally, variations in volcanic output might be internally forced within the mantle (Shinevar et al., 2019; Parnell-Turner et al., 2020), which could be periodic (or at least episodic) and which may vary in period, phase and amplitude from one segment to the next. If so, then the stacking analysis of Goff et al. (2018) would not detect such signals.

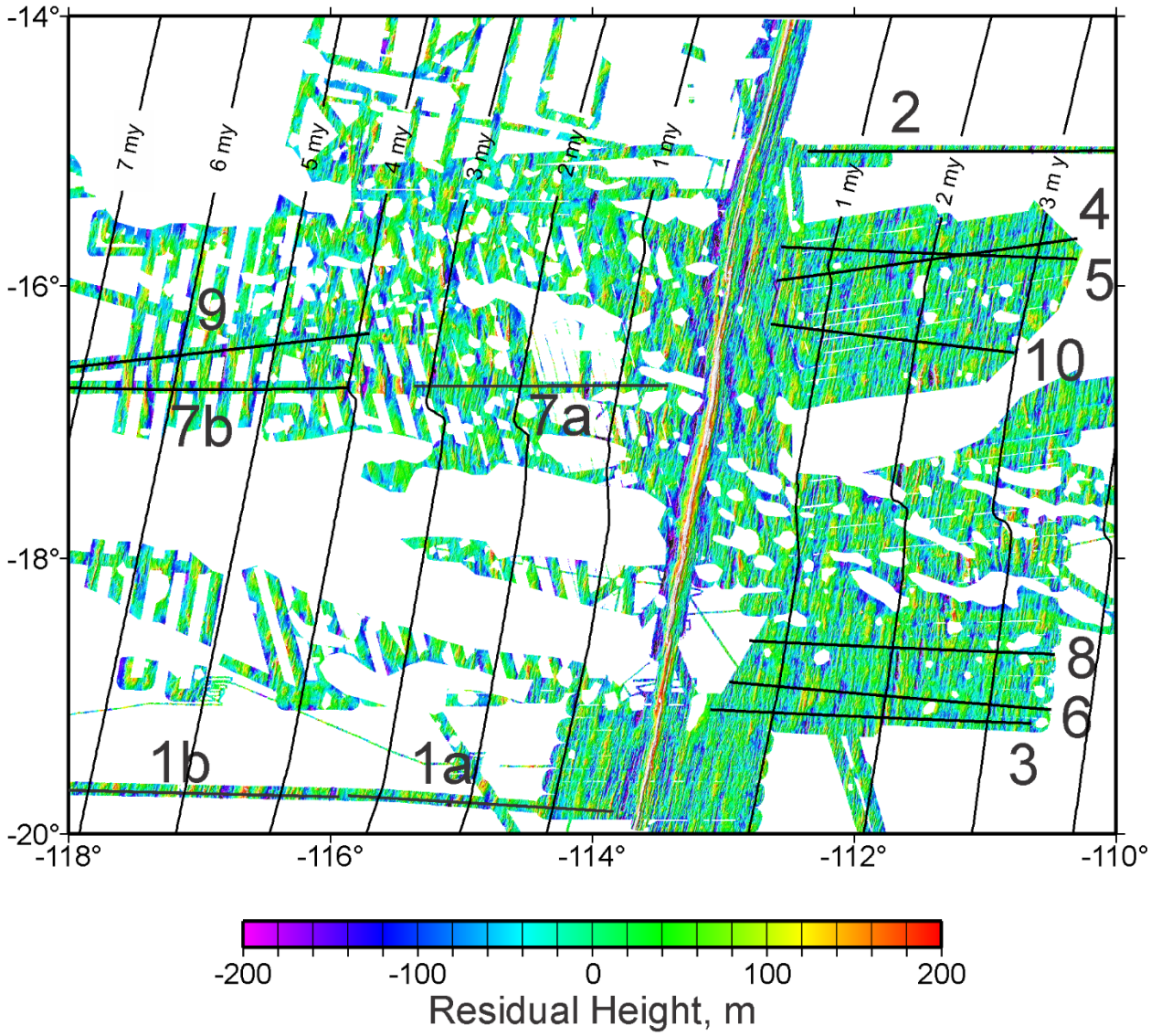

Figure 5. Multibeam bathymetry along the flanks of the southern East Pacific Rise, high-pass filtered with a 40 km box filter and masked to removed seamounts (modified from Goff et al., 2018). Crustal ages are contoured at 1 my increments (Muller et al., 2016; Goff et al., 2018). Profiles used for analysis are indicated by thick black lines and numbered identifiers.

To search for possible temporal periodicities, I have selected 12 profiles of residual height (Figure 5) and converted to age versus residual height using the crustal age model presented in Goff et al. (2018). Each profile is ~2.5-3 my long, resampled at a uniform interval of 0.0025 my, and linearly interpolated over any gaps in coverage. Such gaps were few as profiles were carefully selected to correspond to

swaths of nearly complete coverage and no seamounts. Profiles were also restricted to ages > 0.5 my to avoid the MOR axial high and associated negative sidelobes that form with the high-pass filter of the original bathymetry.

For example purposes, I present here the full analysis of Profile 7a (Figures 6 and 7), which is one of the more convincing detections of a periodic component. The full suite of profiles analyses are presented in the Supplementary Material, with results listed in Table 1. The age-versus-residual height values for Profile 7a are shown in Figure 6a, and its sample autocovariance function is shown in Figure 6b. A von Kármán model is fit to the sample autocovariance (Figure 6b) via weighted, least-squares inversion as formulated in Goff and Jordan (1988). The estimated value for RMS height, H, is 61.1 ± 4.7 m, and the scale parameter, k_0, is 68.3 ± 13.8 my^{-1}. Estimation of the parameter ν tends to become unstable as it approaches its upper limit of 1 (Goff, 1991); that was the case here and in most of the estimations in this analysis, and was assumed to be 0.9. A characteristic time, λ_0, can be defined by the width, or second moment of the autocovariance model (Goff and Jordan, 1988):

$$\lambda_0 = \frac{\sqrt[2]{2(\nu+1/2)}}{k_0}. \quad (16)$$

The characteristic time roughly corresponds to the visually dominant (on average) peak-to-peak distance (Goff, 1991), and thus is an important point of comparison for any potential identification of a harmonic component. For Profile 7a, λ_0 = 0.049 ± 0.010 my (which equates to ~3.8 km). The tail of the sample autocovariance (Figure 6b) exhibits a number of evidently regularly-space peaks and troughs that strongly suggest the presence of a harmonic component to the profile.

The spectral analysis of Profile 7a is shown in Figure 7. The sample power spectrum (Figure 7a) follows the modeled von Kármán power spectrum well at lower frequencies, but deviates at the higher frequencies. This deviation from the power law trend is a phenomenon noted by Goff and Jordan (1988), who attributed it to the “response”, or beam width of the multibeam echosounder being larger than the sample interval. This effect may also be caused by the averaging associated with the gridding

process. In any case, it is not a concern in this analysis because any periodic elements at that scale would exhibit very small amplitudes. In addition to the overall von Kármán-like trend, a noticeable peak is observed corresponding to a period of 0.145 my, approximately three times the characteristic time of the best-fitting von Kármán model. That same peak is shown on the empirically pre-whitened spectrum (Figure 7b) to be significant at a very high level of confidence: 5.1σ. Therefore, it can be stated that a periodic signal, with period of 0.145 my, is present in Profile 7a with a very high degree of certainty.

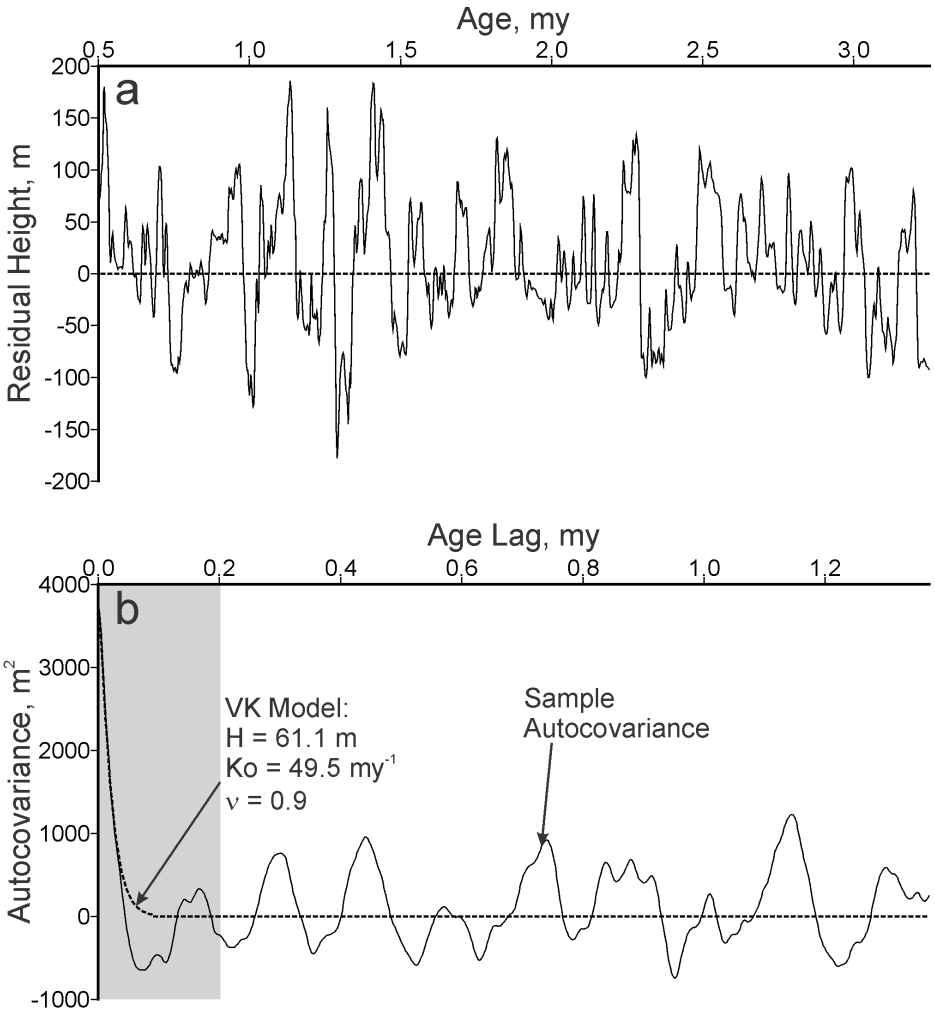

Figure 6. (a) Bathymetric profile 7a converted from distance to age on the x-axis using the age model of Goff et al. (2018); location shown in Figure 5. (b) Sample autocovariance (solid) computed from (a), with best-fit von Kármán model (dashed). The power spectral density in Figure 7a is computed by discrete Fourier transform of the full sample autocovariance (with Hermetian symmetry), whereas the empirically pre-whitened spectrum in Figure 7b is computed in the same way after zeroing out the shaded region that fully encompasses the structural (non-zero mean) portion of the autocovariance and tapering the edges.

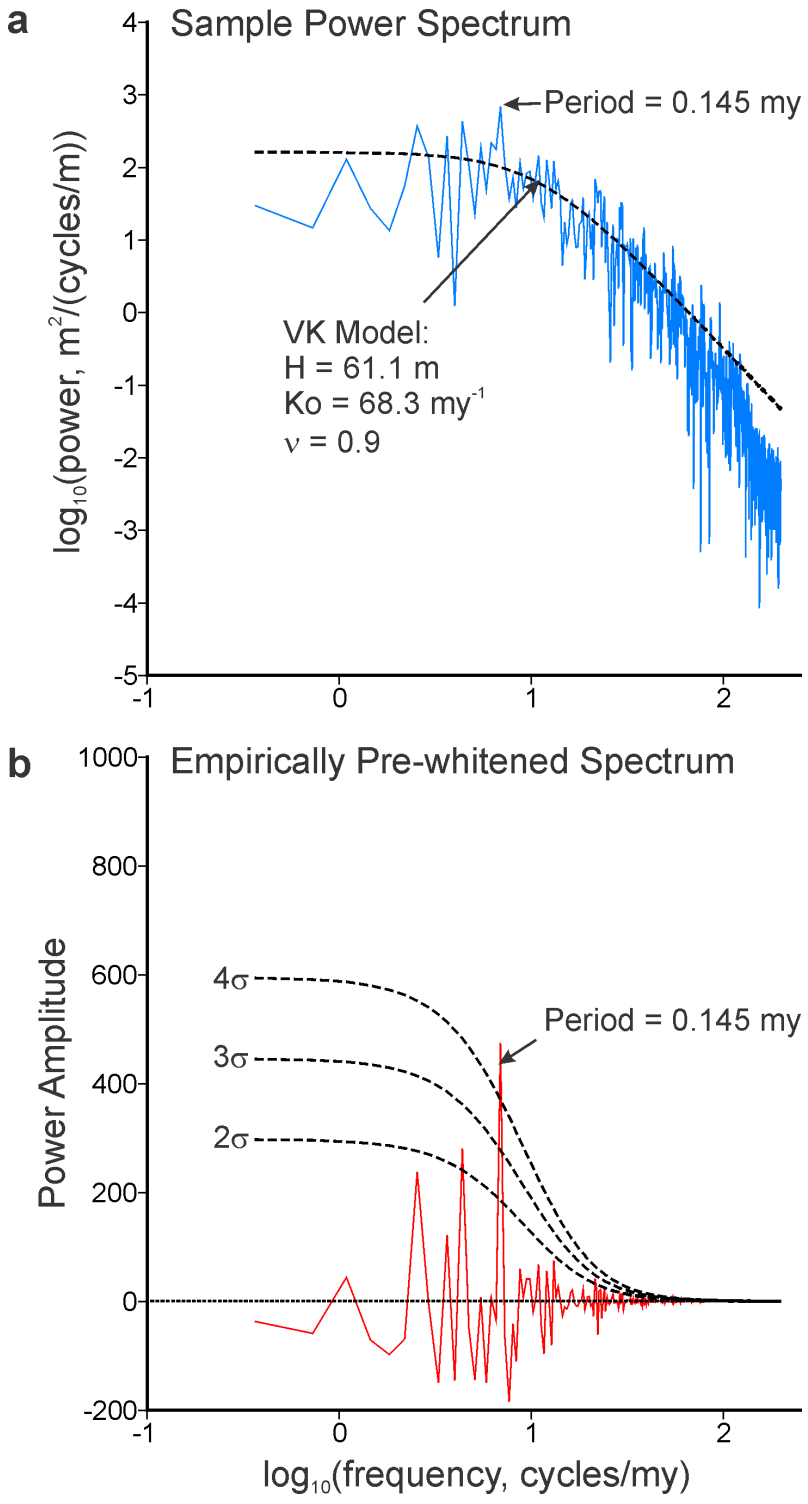

Figure 7. (a) Sample power spectrum and (b) empirically pre-whitened spectrum calculated from the sample autocovariance of Profile 7a shown in Figure 6b. The best-fit von Kármán model is overlain on the power spectral density, and the 2σ, 3σ, and 4σ upper bounds on the null hypothesis are overlain on the empirically pre-whitened spectrum. One harmonic component at a period of 0.145 my is detected at 5.1σ confidence

Having identified a likely periodic signal, the next step is to estimate its amplitude, α. That value can be estimated from the amplitude of the peak observed on the empirically pre-whitened spectrum, which is proportional to α^2 (Priestley, 1981). However, the coefficient is a complex function of *N*, *m* and the tapers used prior to DFT of $\hat{P}_X^m(f)$. Priestly (1981) calculated closed-form approximations for linear or no tapers, neither of which I found appropriate to the application at hand. Rather than attempt the same calculation for the $\cos^2$ tapers used here, a far simpler method is to generate a simple cosine function and pass it through the same spectral analysis applied to the data profile. Then, α is adjusted until the height of the resulting spectral peak matches what is observed on the empirically pre-whitened spectrum. With this procedure I estimated α to be ~30 m for the 0.145 my period peak detected for Profile 7b. The variance of this sinusoidal contribution is $\alpha^2/2$ = 450 m^2, which equates to an RMS of 21.2 m. The overall variance of Profile 7a is H^2 = 3730 m^2. Therefore, 3730 m^2 - 450 m^2, or 3280 m^2 of the total variance of Profile 7a, is attributed to the aperiodic component of the profile. This equates to an RMS of 57.3 m, and which is 2.7 times the RMS of the sinusoidal component. Thus, while significant in its measurability, the sinusoidal contribution at 0.145 my period represents a relatively minor component of Profile 7a compared to the aperiodic signal.

I next test the ability of the mixed spectrum statistical model, of the form presented in Equation (15), to match these observations. To do so I formulated a synthetic profile composed of: (1) a von Kármán aperiodic component using the parameters *H* = 57.3 m (the estimated RMS height of the aperiodic component, rather than the overall RMS), and k_0 and ν as derived from the best-fit model, and (2) an added cosine function corresponding to amplitude 30 m and period 0.145 my. Initially this created a spectral peak that was too large, so the amplitude was reduced to 24 m to match the height exactly. This reiterates the point that the estimation of harmonic amplitude has significant uncertainties owing to modulation by the random, aperiodic component of the spectrum. The level of uncertainty will depend on the variation of the empirically pre-whitened continuous spectrum in proportion to the

418 height of the discrete spectral peak at the frequency of interest. The synthetic profile and sample
419 autocovariance are shown in Figure 8, and the resulting spectral analysis is shown in Figure 9. The
420 similarity of these plots to Figures 6 and 7, respectively, is very strong, particularly in the self-evident
421 harmonic component in the tail of the sample autocovariance (Figure 8b), and in the size spectral peaks
422 noted both on the sample power spectrum (Figure 9a) and the empirically pre-whitened spectrum
423 (Figure 9b). The only notable difference between real and synthetic is in the power at the highest
424 frequencies (Figures 7a versus 9a), which causes the real profile (Figure 6a) to have a smoother
425 appearance than the synthetic profile (Figure 8a) at the smallest scales.

426 Spectral analysis plots for all twelve profiles are presented in the Supplementary Material. Estimated
427 von Kármán and cosine function parameters from each analysis are listed in Table 1. Periodicities were
428 detected in all but three of the profiles, and in several there were multiple periodicities detected. The
429 periods detected were highly variable, however, ranging at least an order of magnitude from 0.02 my
430 (the minimum considered for inclusion in Table 1) to 0.216 my. There is no evident clustering of values
431 at the Milankovitch periods of 0.100 my, 0.041 my or 0.026 my, although there are several detected
432 periods that are equal or close to those values. More importantly, there is no evidence of spatial or
433 temporal consistency. For example, Profiles 3, 6 and 8 are quite proximal (Figure 5), but exhibit no
434 consistency in the periods of their harmonic components (Table 1). The same inconsistency is also true
435 of Profiles 1a and 1b, and Profiles 7a and 7b (Table 1), although each pair is sited along the same flow
436 line (Figure 5) and so were generated at the same ridge crest segment but at different times.

437 To gauge the significance of each detected periodicity to variability of each profile, I calculate a
438 value *R* as the ratio of RMS heights of the periodic to aperiodic components, respectively. By this
439 measure (Table 1), there is a clear separation of significance between those harmonic detections with
440 periods greater than or less than the characteristic time of the best-fitting von Kármán model. Those
441 periods greater than the characteristic time, seven in all, exhibit *R* values ranging from 0.19 to 0.38, with

all but the smallest of those >0.27. In contrast, periods less than the characteristic time exhibit *R* values ranging from 0.03 to 0.11, with only the largest > 0.08. In all cases, however, the aperiodic component of the profiles is the dominant source of variability.

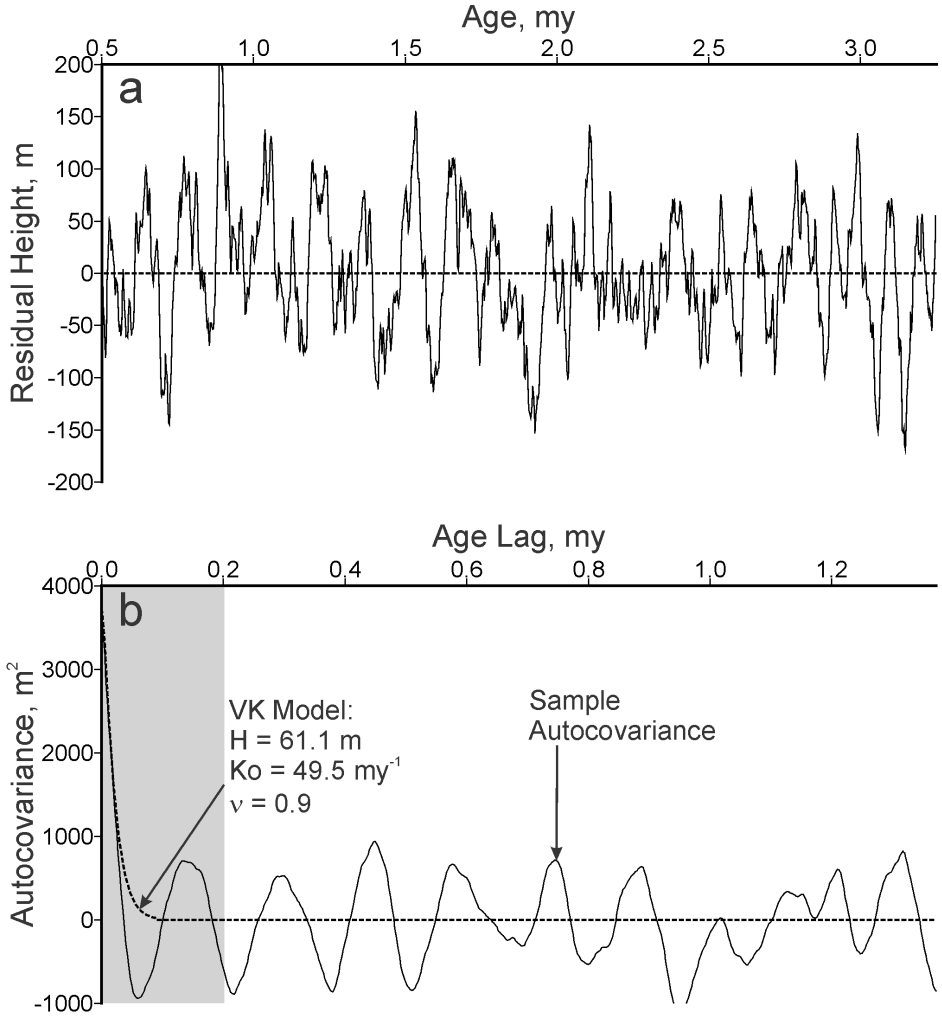

Figure 8. (a) Synthetic profile formed from the summation of (1) an aperiodic von Kármán profile, with parameters as noted in the text, and (2) a cosine function of amplitude 24 m and period 0.145 my. (b) Sample autocovariance (solid) computed from (a), with best-fit von Kármán model for Profile 7a (dashed). The power spectral density in Figure 9a is computed by discrete Fourier transform of the full sample autocovariance (with Hermitian symmetry), whereas the empirically pre-whitened spectrum in Figure 9b is computed in the same way after zeroing out the shaded region that fully encompasses the structural (non-zero mean) portion of the autocovariance and tapering the edges.

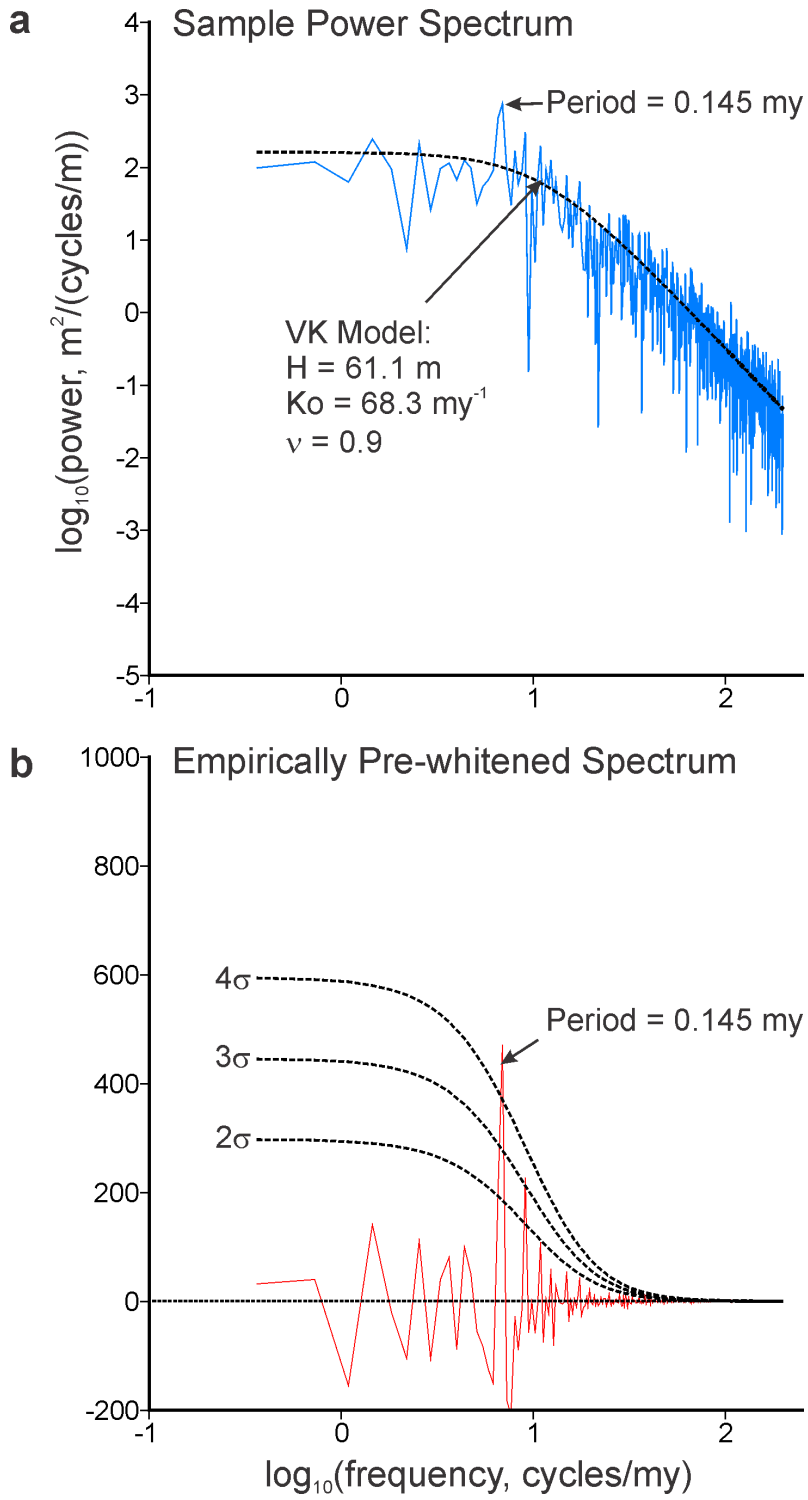

455

456 Figure 9. (a) Sample power spectrum and (b) empirically pre-whitened spectrum calculated from the
457 sample autocovariance of the synthetic profile shown in Figure 8. The best-fit von Kármán model is
458 overlain on the power spectral density, and the 2σ, 3σ, and 4σ upper bounds on the null hypothesis are
459 overlain on the empirically pre-whitened spectrum. The height of the spectral peak at 0.145 my period,
460 observed in spectral analysis of Profile 7a (Figure 7), is successfully reproduced by the synthetic profile.

461

462 **5. Conclusions and Discussion**

463 Application of an "empirical pre-whitening" spectral analysis, based on the "P(λ) test"
464 formulated by Priestly (1981), has enable detection of temporal periodicities at high confidence in a
465 number of profiles sampled from multibeam bathymetric data along the southern EPR. However, these
466 harmonic signals are relatively minor components of the overall variability of the profiles, which are
467 instead dominated by an aperiodic signal conforming to a continuous, rather than discrete spectrum.
468 Furthermore, the periods expressed by the harmonic signals are widely variable, and do not exhibit any
469 spatial or temporal consistency. This behavior makes the origin of harmonic signals in abyssal hill
470 morphology enigmatic, but does rule out external forcing such as may be applied by Milankovich cycle-
471 based variability in sea level. Rather, the forcing must be internal, highly localized, and subject to
472 changing conditions over time.

473 Abyssal hills generated at fast spreading rates are predominantly fault-bounded, horst-and-graben
474 structures (e.g., Macdonal et al., 1996; Macdonald, 2015). Furthermore, fault scaling parameters
475 (spacing, length, throw) are successfully modeled as random distributions constrained by scaling laws
476 (Malinverno and Cowie, 1993; Bohnenstiehl, and Carbotte, 2001). The dominant aperiodic component
477 of abyssal hills can thus reasonably be assumed to be associated with this fault-generated morphology,
478 characterized statistically by a von Kármán model defined by parameters RMS height, characteristic
479 time, and fractal dimension. The most significant harmonic contributions to abyssal hills, typically with
480 RMS heights around a quarter to a third of the aperiodic RMS, exhibit periods that are larger than the
481 characteristic time. Such variations in bathymetry could plausible be associated with variations in crustal
482 thickness associated with temporal variations in magma supply (Canales et al., 2000; Shinevar et al.,
483 2019; Parnell-Turner et al, 2020). Parnell-Turner et al. (2020), in a spectral analysis of abyssal hill
484 morphology on the flanks of the medium-spreading-rate Southeast Indian Ridge, also discerned a scale

of morphology (although no clear indication of periodicity) that was larger than the characteristic time/width of abyssal hills. They hypothesize that variations in melt supply at <0.2 my time scales could be associated either with time-varying, melt rich "porosity waves" in the mantle, or by small-scale mantle heterogeneities. Investigating whether these or other mechanisms could apply to the super-fast spreading southern EPR would be an important avenue of investigation for a modeling effort (though beyond the scope of this paper). These results provide key observations that need to be accounted for in any such effort, including the range of periods observed, their spatio-temporal variability, and their topographic amplitudes.

Acknowledgements. The southern East Pacific Rise multibeam data used in this analysis are available from the Global Multi-Resolution Topography Data Synthesis (https://www.gmrt.org/).

References

Babadi, B., and Brown, E.N. (2014). A review of multitaper spectral analysis. *IEEE Transactions on Biomedical Engineering, 61*, 1555-1564.

Bhansali, R.J. (1979). A mixed spectrum analysis of lynx data. *Journal of the Royal Statistical Society Series A, 142*, 199-209.

Bohnenstiehl, D. R., & Carbotte, S. M. (2001). Faulting patters near 19°30'S on the East Pacific Rise: Fault formation and growth at a superfast spreading center. *Geochemistry, Geophysics and Geosystems, 2*(9), doi: 10.1029/2001GC000156.

Canales, J. P., Collins, J. A., & Detrick, R. S. (2000). Seismic structure across the rift valley of the Mid-Atlantic Ridge at 23°20' (MARK area): Implications for crustal accretion processes at slow spreading ridges. *Journal of Geophysical Research, 105*, 28411–28425.

Crowley, J. W., Katz, R. F., Huybers, P., Langmuir, C. H., & Park, S.-H. (2015). Glacial cycles drive variations in the production of oceanic crust. *Science, 347*, 1237-1240.

DeMets, C., Gordon, R. G., Argus, D. G., & Stein, S. (1990). Current plate motions. *Geophysical Journal, 101*(2), 425-478.

Durant, C., Ballu, V., Gente, P., & Dubois, J. (1996). Horst and graben structures on the flanks of the Mid-Atlantic ridge in the MARK area (23°22'N): Submersible observations. *Tectonophysics, 265*, 275-297.

Garrido, J., and Garcia, J.A. (1992). Periodic signals in Spanish monthly precipitation data. *Theoretical and Applied Climatology*, 45, 97-106.

Goff, J.A. (1995). Quantitative analysis of sea-ice draft I: Methods for stochastic modeling. J. Geophys. *Journal of Geophysical Research, 100*, 6993-7004.

Goff, J. A., & Jordan, T. H. (1988). Stochastic Modeling of Seafloor Morphology: Inversion of Sea Beam Data for Second-Order Statistics. *Journal of Geophysical Research: Solid Earth*, *93*, 13589–13608.

519 Goff, J. A., & Tucholke, B.E. (1997). Multi-scale spectral analysis of bathymetry on the flank of the
520 MidAtlantic Ridge: Modification of the seafloor by mass wasting and sedimentation. *Journal of*
521 *Geophysical Research, 102*, 15,447-15,462.
522 Macdonald, K. C. (1982). Mid-ocean ridges: Fine scale tectonic, volcanic and hydrothermal processes
523 within the plate boundary zone. *Annual Reviews of Earth and Planetary Science, 10*, 155-190.
524 Macdonald, K. C. (2015). Milankovich sea level-change pumping of fault slip may enhance abyssal hill
525 growth, with spacing control by melt pumping or elastic properties. *AGU Fall Meeting*, V24A-05.
526 Malinverno, A., & Cowie. P. A. (1993). Normal faulting and the topographic roughness of mid-ocean
527 ridge flanks. *Journal of Geophysical Research, 98*, 17,921-17,939.
528 Mann, M.E., and Lees, J.M. (1996). Robust estimation of background noise and signal detection in
529 climate time series. *Climate Change, 33,* 409-445.
530 McCoy, E.J., Walden, A.T., and Percival, D.B. (1998). Multitaper spectral estimation of power law
531 processis. *IEEE Transactions on Signal Processing, 46*, 655-668.
532 Müller, R. D., Seton, M., Zahirovic, S., Williams, S. E., Matthews, K. J., Wright, N. M., Shephard, G. E.,
533 Maloney, K. T., Barnett-Moore, N., Hosseinpour, M., Bower, D., J., & Cannon, J. (2016). Ocean basin
534 evolution and global-scale plate reorganization events since Pangea breakup. *Annual Reviews of*
535 *Earth and Planetary Science, 44*, 107-138.
536 Olive, J.-A., Behn, M. D., Ito, G., Buck, W. R., Escartín, J., & Howell, S. M. (2016). Response to Comment
537 on “Sensitivity of seafloor bathymetry to climate-driven fluctuations in mid-ocean ridge magma
538 supply.” *Science, 352*, 2–4.
539 Parnell-Turner, R., Sim, S.J., & Olive, J.-A. (2020). Time-dependent crustal accretion on the Southeast
540 Indian Ridge revealed by Malaysia Airlines flight MH370 search. *Geophysical Research Letters*, in
541 press, doi: 10.1029/2020GL087349.

542 Percival, D.B., & Walden, A.T. (1993). *Spectral Analysis for Physical Applications: Multi-tape and*
543 *Conventional Univariate Techniques*. Cambridge University Press, Great Britain, 583 pp.
544 Priestley, M.B. (1981). *Spectral Analysis and Time Series*. Academic Press, San Diego, California, 890 pp.
545 Scheirer, D. S., Macdonald, K. C., Forsyth, D. W., Miller, S. P., Wright, D. J., Cormier, M.-H., & Weiland, C.
546 M. (1996). A Map Series of the southern East Pacific Rise and its flanks, 15°S to 19°S. *Marine*
547 *Geophysical Research, 18*(1), 1-12.
548 Shinevar, W.J., Mark, H.F., Clerk, F., Codillo, E.A., Gong, J., Olive, J.-A., Brown, S.M., Smalls, P.T., Liao, Y.,
549 Le Roux, V., & Behn, M.D. (2019). Causes of oceanic crustal thickness oscillations along a 74-m Mid-
550 Atlantic Ridge flow line. Geochemistry, Geophysics, Geosystems, 20, 6123-6139.
551 Tolstoy, M. (2015). Mid-ocean ridge eruptions as a climate valve. *Geophysical Research Letters, 42*(5),
552 doi: 10.1002/2014GL063015.
553 Thomson, D.J. (1990). *Time series analysis of Holocene climate data. Philisophical Transactions of the*
554 *Royal Society of London Series A*, 330, 601-616.
555 Vaughn, S. (2005). A simple test for periodic signals in red noise. *Astronomy and Astrophysics, 431*, 391-
556 403.
557 von Kármán, T. (1948). Progress in the statistical theory of turbulence. *Journal of Marine Research, 7*,
558 252–264.
559
560

Table 1. Modeled aperiodic and detected periodic components of southern EPR profiles

Profile	H, m	λ_0, my	Period, my (min 0.02)	Z_σ (> 3.5)	α, m	R
1a	65.5	0.065	0.112	4.6	25	0.28
			0.021	3.9	3	0.03
1b	83.8	0.089	0.037	3.9	7	0.06
2	74.1	0.050	0.143	5.3	35	0.35
			0.042	4.0	11	0.11
3	51.3	0.038	0.111	3.9	19	0.27
			0.082	6.2	20	0.29
4	50.4	0.049	-	-	-	-
5	50.3	0.043	0.032	3.7	6	0.08
			0.027	6.2	6	0.08
6	48.2	0.056	0.216	4.2	24	0.38
			0.022	4.8	3	0.05
7a	68.3	0.049	0.145	5.1	30	0.33
7b	80.3	0.068	-	-	-	-
8	41.3	0.034	0.047	4.1	11	0.19
9	58.4	0.065	0.040	3.7	7	0.08
			0.030	4.0	5	0.06
			0.025	7.4	5	0.06
			0.020	6.0	4	0.05
10	55.5	0.034	-	-	-	-

H: RMS height of best-fit von Kármán model

λ_0: Characteristic time of best-fit von Kármán model

Z_σ: Height of spectral peak expressed as multiple of standard deviation σ.

α: Estimated amplitude of harmonic component.

R: Ratio of periodic to aperiodic RMS

-: No detection of harmonic component